Signatures of Cold Ions in a Kinetic Simulation of the Reconnecting Magnetopause

Jérémy Dargent, Nicolas Aunai, B. Lavraud, Sergio Toledo-Redondo, F. Califano

To cite this version:

Jérémy Dargent, Nicolas Aunai, B. Lavraud, Sergio Toledo-Redondo, F. Califano. Signatures of Cold Ions in a Kinetic Simulation of the Reconnecting Magnetopause. Journal of Geophysical Research Space Physics, 2019, 124 (4), pp.2497-2514. ⟨10.1029/2018JA026343⟩. ⟨hal-02345138⟩

JGR Space Physics

RESEARCH ARTICLE
10.1029/2018JA026343

Signatures of Cold Ions in a Kinetic Simulation of the Reconnecting Magnetopause

J. Dargent[1,2,3], **N. Aunai**[3], **B. Lavraud**[2], **S. Toledo-Redondo**[2,4], and **F. Califano**[1]

[1]Physics Department "E. Fermi", University of Pisa and CNISM, Pisa, Italy, [2]IRAP, Université de Toulouse, CNRS, UPS, CNES, Toulouse, France, [3]LPP, CNRS, Ecole polytechnique, Sorbonne Université, Univ. Paris-Sud, Observatoire de Paris, Université Paris-Saclay, PSL Research University, Palaiseau, France, [4]European Space Agency, ESA/ESAC, Madrid, Spain

Key Points:
- We make PIC simulations of asymmetric magnetic reconnection including both hot and cold magnetospheric ion populations
- We study cold ions' specific signatures along magnetospheric separatrices
- We develop a theoretical model for the crescent-shaped distribution functions of cold ions observed along the separatrices separatrix

Correspondence to:
J. Dargent,
jeremy.dargent@lpp.polytechnique.fr

Citation:
Dargent, J., Aunai, N., Lavraud, B., Toledo-Redondo, S., & Califano, F. (2019). Signatures of cold ions in a kinetic simulation of the reconnecting magnetopause. *Journal of Geophysical Research: Space Physics*, *124*, 2497–2514. https://doi.org/10.1029/2018JA026343

Received 6 DEC 2018
Accepted 14 MAR 2019
Accepted article online 18 MAR 2019
Published online 4 APR 2019

Abstract At the Earth's magnetopause, a low-energy ion population of ionospheric origin is commonly observed at the magnetospheric side. In this work we use a 2-D fully kinetic simulation to identify several original signatures related to the dynamics of cold ions involved in magnetic reconnection at the asymmetric dayside magnetopause. We identify several original signatures of the cold ions dynamics driven by the development of magnetic reconnection at the asymmetric dayside magnetopause. We find that cold ions tend to rarefy in the diffusion region, while their density is enhanced as a result of compression along magnetospheric separatrices. We also observe the formation of crescent-shaped cold ion distribution functions along the separatrices in the near-exhaust region, and we present an analytical model to explain this signature. Finally, we give evidence of a localized parallel heating of cold ions. These signatures should be detected with the magnetospheric multiscale mission high-resolution observations.

1. Introduction

Since the launch of the Cluster mission, observations of magnetopause crossings often reveal the presence of a cold magnetospheric ion population in addition to the hot magnetospheric ion populations (André et al., 2010; Fuselier et al., 2016; McFadden et al., 2008; Sauvaud et al., 2001). Due to their low energy, these ions (hereafter cold ions) are in general not observed because of the finite low energy limit of particle instruments and the generally positive and nonnegligible spacecraft potential (Lavraud & Larson, 2016; McFadden et al., 2008; Sauvaud et al., 2001). However, they usually become detectable thanks to their acceleration by nearby magnetopause motions (McFadden et al., 2008; Sauvaud et al., 2001).

When present, cold magnetospheric ions represent an important component of the magnetospheric plasma density. Their density is usually of the same order as hotter ions from the ring current (André & Cully, 2012). In the case of plasmaspheric plume events, the density can even be higher than the magnetosheath density (Walsh et al., 2014). As such, they must play a key role in the properties and dynamics of magnetopause magnetic reconnection. Though plasmaspheric plumes have been shown to have a significant mass loading effect on the reconnection rate (Borovsky & Denton, 2006; Walsh et al., 2013), recent works suggest that cold ions also have a significant impact on magnetic reconnection because of their temperature (André et al., 2016; Toledo-Redondo et al., 2015, 2018).

Cold ions are heated and accelerated in the separatrix region (Divin et al., 2016; Toledo-Redondo, André, Vaivads, et al.,2016; Toledo-Redondo et al., 2017, 2018). Once in the exhaust, they mix with magnetosheath ions and, therefore, become hard to distinguish from other ions in spacecraft data (André et al., 2016; Li et al., 2017; Toledo-Redondo et al., 2015). Owing to this heating, cold ions take part in the energy budget of magnetic reconnection (Aunai et al., 2011) in some yet unknown proportion. A recent study based on four independent observations by MMS of the reconnecting magnetopause with cold ions showed that cold ions take at least 10–25% of the energy spent into particle heating (Toledo-Redondo et al., 2017). To study cold ion heating, numerical simulations have the advantage of being able to flag ions and then discriminate cold ions from other populations, even once heated.

In this work, we present a 2-D fully kinetic simulation of asymmetric magnetic reconnection with two ion populations on the magnetospheric side: a hot one and a cold one. In particular, we highlight several specific signatures of magnetospheric cold ion dynamics at the reconnecting magnetopause.

The present paper is organized as follows. Section 2 introduces the setup of the simulation. Section 3 presents the results and discusses the cold ion signatures. It is itself split into three parts. Section 3.1 shows and explains the macroscopic behavior of cold ions in the vicinity of the reconnection region. Section 3.2 points out a signature marking the cold ion distribution functions (DFs) at the magnetospheric separatrix, namely, a crescent-shaped distribution, and proposes an analytical model to explain it. Finally, in section 3.3, we compare the DFs for each ion population and present a cold ion heating observed along separatrices. In section 4, we discuss the results, and in section 5 we present a summary and some potential use of the described signatures.

2. Simulation Setup

We have performed a numerical simulation of collisionless asymmetric magnetic reconnection with cold ions in a two-dimensional (2-D) spatial geometry, using the fully kinetic particle-in-cell code SMILEI (Derouillat et al., 2017). This is the same simulation presented in Dargent et al. (2017). All quantities are normalized using ion (i.e., proton) scale quantities. The magnetic field and density are normalized to B_0 and n_0, respectively, arbitrarily fixed to magnetosheath values. The masses and charges are normalized to the ion mass m_p and charge e; time is normalized to the inverse of the proton gyrofrequency ω_{ci}^{-1} and length to the proton inertial length δ_i. Velocities are normalized to the Alfvén velocity v_{Al}. Temperature is normalized to $k_B T_0 = B_0^2/n_0\mu_0$.

The simulation is performed in the (x, y) plane in a domain of size $(x_{max}, y_{max}) = (320, 128)\,\delta_i$. There are $n_x = 6{,}400$ cells in the x direction, $n_y = 5{,}120$ cells in the y direction, and initially 50 particles per cell and per population. The time step is $dt = 8.4 \cdot 10^{-4}$. The ion to electron mass ratio is 25, and the electron to mean ion temperature ratio is constant and chosen equal to $\theta = T_e/T_i = 0.2$. We fix the Alfvén velocity to $v_{Al} = 0.05c$, where c is the speed of light. The initial condition is given by a double asymmetric current sheet with periodic boundary conditions. The two layers have a width of $L = 1$ and do not interact with each other, even at later times. From now, we will only focus on one layer, on which magnetic reconnection is initiated with a small magnetic perturbation. The magnetic mean field $\mathbf{B} = B_x(y)\mathbf{e}_x$ varies from −1 on the magnetosheath side to 2 on the magnetospheric side:

$$\mathbf{B}(x, y) = \frac{1}{B_r}\left[-\tanh\left(\frac{y - y_0}{L} + arctanh\left(\frac{B_r - 1}{B_r + 1}\right)\right)\frac{B_r + 1}{2} - \frac{B_r - 1}{2}\right]\mathbf{u}_x, \tag{1}$$

with $B_r = |B_{sheath}/B_{sphere}| = 0.5$ the magnetic field ratio between both sides of the current sheet, y_0 the position of the layer, and $\mathbf{u}_x$ the unit vector in the x direction. The density n varies from 1 on the magnetosheath side to 1/3 on the magnetospheric side:

$$n(x, y) = \frac{1}{n_r}\left[1 + \frac{n_r - 1}{2}\left(\tanh\left(\frac{y - y_0}{L}\right) + 1\right)\right], \tag{2}$$

with $n_r = n_{sheath}/n_{sphere} = 3$ the density ratio between both sides of the current sheet. We focus on simulation outputs at $t = 120$ when reconnection has reached a steady state.

The magnetosphere density is composed by two thirds of cold ions and one third of hot ions. The temperature of each ion population, that is, T_{ish} for magnetosheath ions and T_{ic} and T_{ih} for cold and hot magnetospheric ions, respectively, is assumed constant, so that the total ion temperature $T_i = \frac{1}{n}\sum n_{i,s}T_{i,s}$ variation only depends on the density variation of each ion population. With this assumption, we just need equation (2) and to fix a density profiles for magnetosheath ions to obtain the initial density profiles for each ion population and the global temperature of ions (Dargent et al., 2017):

$$n_{ish}(x, y) = \frac{1}{2}\left[1 + \tanh\left(\frac{y - y_0}{L}\right)\right], \tag{3}$$

$$n_{ic}(x, y) = \frac{T_{hoc}}{1 + T_{hoc}}\left[\frac{1}{T_{ih}}\left(\frac{K - B^2/2}{1 + \theta} - n_{ish}T_{ish}\right) + n_{ish} - n\right], \tag{4}$$

$$n_{ih}(x, y) = n - n_{ish} - n_{ic}, \tag{5}$$

where $n_{hoc} = n_{ih}/n_{ic} = 0.5$ and $T_{hoc} = T_{ih}/T_{ic} = 500$ are the hot over cold asymptotic density and temperature ratio, respectively. K is the constant in the pressure balance equation, and we arbitrarily fix

Table 1
Asymptotic Values of the Fields Normalized to Ion Characteristic Quantities

Quantities	B_x	n	T_i	T_{ish}	T_{ic}	T_{ih}
Magnetosphere	2	0.333	5	0	0.03	14.9
Magnetosheath	−1	1	2.9	2.9	0	0

it at $K = B_r^2/2$. The asymptotic values of the different quantities are summarized in Table 1. To compare with spacecraft data, we have to fix the magnetic field and density (e.g., $B_0 = 20$ nT and $n_0 = 4$ cm^{-3} in the magnetosheath), and we set $k_BT_0 \approx 7.9610^{-17}$ J ≈ 497 eV. This means $T_{ish} \approx 1.4$ keV, $T_{ih} \approx 7.2$ keV and $T_{ic} \approx 14$ eV, which are realistic values.

3. Cold Ion Signatures

3.1. Cold Ion Rarefaction and Compression

In Figure 1, we show a zoom of the simulation box around the magnetic reconnection region at $t = 120$. The X point is located at about $(x, y) = (160, 32)$. Figure 1a shows E_y, the electric field normal to the current layer (hereafter called normal electric field). The magnetic field lines represented on this figure allow us to visualize the X point and the separatrices. We notice in particular that the magnetospheric separatrix is colocated with a strong positive electric field: the Hall electric field. We will hereafter call this region the Hall electric field region. In Figure 1b, we show the density of cold ions together with the cold ion bulk streamlines. We observe that the density of cold ions around the separatrix is quite inhomogeneous; in particular near the diffusion region from the magnetospheric side outward, the density quickly decreases, with a clear rarefaction of cold ions before the X point. By contrast, for $x < 140$ and $x > 180$, the density tends to increase along separatrices. This feature remains true all along the separatrices in the whole simulation box. When reaching the magnetopause, the streamlines diverge on both sides of the X point and accumulate along the magnetospheric separatrices. Correspondingly, the cold ion density drops close to the X line as the streamlines diverge and increases along separatrices where, on the contrary, streamlines converge. Toledo-Redondo, André, Khotyaintsev, et al.(2016) have also identified a cold ion dropout close to the X line using MMS observations at the reconnecting magnetopause. They explained it with the demagnetization of cold ions and their acceleration parallel to E inside this region, which they named the cold ion diffusion region. This phenomenon is observed here but is not enough to explain the density drop, as the latter begins below the Hall electric field region, in a place where cold ions are still magnetized.

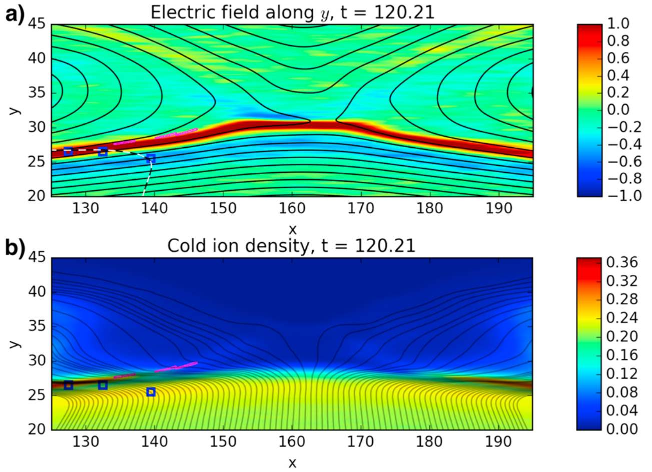

Figure 1. Cold ion density and electric field in the simulation for a zoom around the magnetic reconnection region at $t = 120 \quad \omega_{ci}^{-1}$. (a) Electric field along y. Black lines represent magnetic field lines. The black and white dashed line represents a cold ion streamline. (b) Cold ion density map. The 100 black lines represent cold ion streamlines.The streamlines are calculated from from initial positions regularly distributed along the x axis for $y = 20$. The purple (blue) contours show the positions of particle distributions showed in Figure 2 (Figure 7).

An important feature of magnetospheric cold ions is that they remain frozen in the magnetic field even very close to the separatrix, at a place where other ions are demagnetized (Dargent et al., 2017; Toledo-Redondo et al., 2015). For this reason, they keep having a fluid-like behavior where other ion populations have a kinetic behavior. Cold ions simply drift along $\mathbf{E} \times \mathbf{B}$ while other populations are impacted by kinetic effects, in particular close to the separatrix. Near the X line, cold ions demagnetize while entering the Hall electric field region. Further away from the diffusion region (typically for $x < 135$ and $x > 185$), where the magnetic field amplitude is stronger, they drift through the Hall electric field region while remaining frozen-in. The divergence of the cold ion flow is solely the consequence of their $\mathbf{E} \times \mathbf{B}$ drift. Far from the separatrix, the cold ion (and all other ion populations) drift in y toward the layer comes from the main component of the magnetic field (B_x) and the weak reconnection electric field (E_z). Close to the separatrix, electromagnetic fields are modified by the Hall physics. Here appear a Hall magnetic field B_z and a Hall electric field E_y. The simulation being asymmetric, the Hall field is much stronger on magnetospheric side, as we can see in Figure 1a for the electric field. The electromagnetic Hall fields induce a $\mathbf{E} \times \mathbf{B}$ drift of cold ions along x. Because of the quadrupole structure of the Hall magnetic field, the drift directions along x are opposed depending on their location (left or right) relative to the X point. Thus, because of the Hall electromagnetic field structure, the cold ion drift diverges left and right of the X point. We also expect a drift in the z direction, with possible 3-D effects that cannot be accounted for in the present 2-D simulation.

Because of their $\mathbf{E}\times\mathbf{B}$ drift within Hall fields, we observe a flow divergence of cold ions. But this drift velocity appears to be larger than their thermal velocity. Typically, the exhaust velocity calculated with the Cassak and Shay (2007) formula gives $v_{out} \approx 0.45$ while the cold ion thermal velocity is $v_{ic,th} \approx 0.17$. Consequently, because of its very low temperature, the whole cold ion distribution is shifted much more than its standard deviation, and there are very few (if any) counter-streaming ions. The DFs of cold ions along the separatrices (ex: Figure 7a, d) shows that indeed, in our simulation, the mean velocity of cold ions along x is larger than the thermal velocity and almost no cold ions are counter-streaming. Thus, because of the flow divergence, which depletes the cold ion inflow in the diffusion region, and the very low temperature of cold ion, which prevents their diffusion along magnetic field lines, very few cold ions reach the diffusion region.

We observe in Figure 1b a peak in the cold ion density (as well as a convergence of the cold ion flow) located in the Hall electric field region (Figure 1a). The increase of the cold ion density at the Hall field appears only where cold ions are magnetized. The kinetic behavior of demagnetized cold ions at the separatrix ($135 < x < 185$) is developed in section 3.2. In the region where they are magnetized, cold ions drift in the normal direction with a velocity $v_{y,drift} = (\mathbf{E}\times\mathbf{B})_y/B^2$. When they enter the separatrix region, a strong Hall magnetic field B_z appears, which implies a decrease of $v_{y,drift}$. The decrease of $v_{y,drift}$ impacts the density through the equation of density: $\partial n/\partial t + \nabla\cdot(n\mathbf{v}) = 0$. In our case, the simulation is in a steady state, and we can neglect the first term. The derivative along z is zero because this simulation is 2-D and the variation of n and v_x along x is negligible compared to the variation along y. The continuity equation can therefore be simplified as $\partial(nv_y)/\partial y \approx 0$. So a decrease of the velocity is correlated with an increase of the density, which is observed in Figure 1b. We can notice thanks to the streamlines that this slowdown of cold ions in the y direction is correlated with an acceleration in the x direction along the separatrices: The cold ions get a velocity parallel to the magnetic field. This will be further discussed in section 3.3.

Below the separatrices, in the magnetosphere, one observes another peak of density, larger but with a weaker amplitude. This structure is related to the local pileup of magnetic field. The mechanism behind this field is similar to what happens at the separatrix. In the magnetosphere, the magnetic field tends to pile up along separatrices, which implies an increase of B_x. Cold ions are locally frozen-in and are thus $\mathbf{E}\times\mathbf{B}$ drifting. Thus, an increase of B_x implies a decrease of the cold ion normal velocity ($v_{ic,y}$) and, because of the continuity equation, an increase of the cold ion density.

Because of their temperatures, cold ions remain frozen-in at location where hotter ions are not anymore. Therefore, they develop a specific fluid signature near boundaries such as the separatrices. We showed and explained some of those cold ion signatures, such as the depletion of the cold ion density near the X point or, on the contrary, the increase of their density along the magnetospheric separatrix.

3.2. Cold Ion Crescent-Shaped DFs

We now look at the behavior of cold ions when they demagnetize along a separatrix. In Figure 1, we observed that there are very few cold ions in the exhaust as compared to their density in the magnetosphere. As a result we get a sharp density gradient, located near the Hall electric field region, between the magnetosphere and the exhaust. Since the density gradient is very large, we expect an asymmetry in the DFs of cold ions. Indeed, local DFs result from a mixing of ions whose guiding center can be located either in the magnetosphere with a lot of cold ions, or in the exhaust with a few cold ions. The separatrix is also the location of the Hall electric field, which plays a key role on the cold ion DFs. The sum of these two effects leads to the crescent-shaped DFs shown in Figure 2, as we will discuss in the following.

In Figure 2 we show the crescent-shaped DFs of cold ions in the (v_y, v_z) plane, hereafter called the crescent-shaped signatures or crescent signatures, as well as their location in the simulation box. The DFs are displayed for cold ions only, panels b–d, and for all ions, panels e–g, in order to show that this signature remains observable even when all ions are considered. For comparison, all DFs (b–g) are shown within the same velocity ranges, which implies that the hottest ions are not visible (see panels e–g) because they are located out of the plot. The crescent signature is located in the exhaust at the boundary with the Hall electric field. It tends to disappear at a certain distance from the X line (see panels b and e).

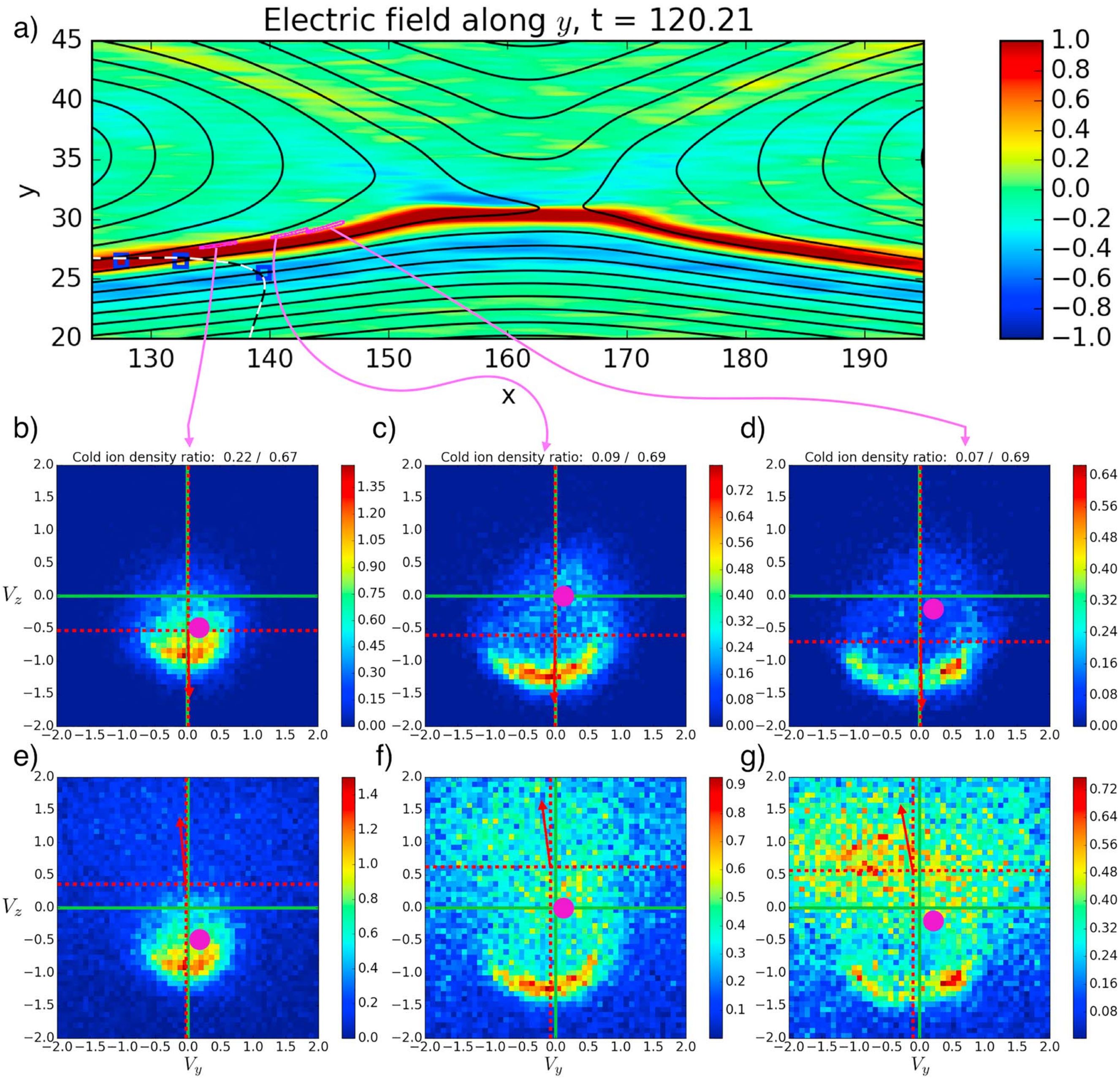

Figure 2. (a) Electric field along y. Black lines represent magnetic field lines. The black and white dashed line represents a cold ion streamline. Blue squares show the location of distribution functions shown in Figure 7. The distribution functions shown in frames b to g are generated with particles located within the thin magenta region, as indicated by the arrows. (b–d) Cold ion distribution functions in the (v_y, v_z) plane. (e–g) All ion distribution functions in the (v_y, v_z) plane. For each distribution the local density ratio of cold ions over all ions is given on top of the column. The distributions are integrated along the v_x axis. Pointed red lines give the mean velocity of the distribution. The red arrow gives the direction of the mean velocity. The purple circle shows the $\mathbf{E} \times \mathbf{B}$ drift velocity.

Two ingredients are necessary to explain this signature. The first is a strong density gradient. If we look at the velocity distribution (v_y, v_z; normal to the magnetic field) for particles located in the Hall electric field layer (in red in Figure 2a), the ions with $v_z < 0$ have their gyrocenter located on the magnetosphere side, and the ions with $v_z > 0$ have their gyrocenter located on the exhaust side. If there are cold ions only on the magnetospheric side of the layer, the distribution has to look like a half disk, similar to Figure 2b. The second ingredient is the Hall electric field. At the location of the distributions of Figure 2, the cold ion energies are significantly higher than in the magnetosphere (cold ion thermal velocity $V_{th} = 0.3$). Indeed, when the particles cross the Hall electric field, they all gain the same amount of energy, leading to a global shift of the

DF and so take the crescent distribution shape, rather that a half-moon distribution shape (see Figures 2c and 2d). These elements are necessary but not sufficient. In order to form such a crescent-shaped DF, some criteria have to be satisfied. If the cold ion population is able to simply drift through the Hall field layer, they will eventually populate the exhaust side of the layer, and the DF will become isotropic. On the other hand, to observe the crescent signature in the exhaust, we need cold ions to cross the Hall field while their gyrocenters remain on the magnetospheric side ($v_z < 0$ for all cold ions). Consequently, this signature has to come from a peculiar orbit of cold ions in the Hall field layer. Furthermore, we do not expect this signature to be observed far from the X line: Where cold ions remain frozen-in while they cross the separatrix, they populate both side of the separatrix. Furthermore, the presence of a relatively dense population of cold ions may possibly hide the presence of a crescent-shaped distribution, even if all the other conditions are satisfied.

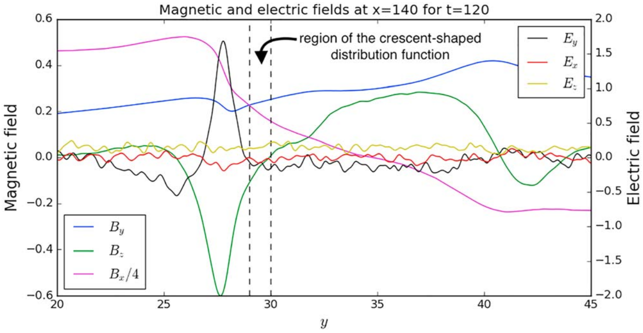

Figure 3. Electric and magnetic field components in the simulation at $t = 120$ for a cut through the layer at $x = 140$. The vertical dashed lines show the y ranges of the selection box used for Figure 2c. The curves are obtained after smoothing the data with 2-D gaussian filter of $\sigma = 1.5$ in the x direction and $\sigma = 0.125$ in the y direction.

In order to model the phenomenon, we first look in Figure 3 at the electromagnetic fields in the simulation through the layer. The cut is done at $x = 140$. The vertical dashed lines show the location of the particle's selection box for the crescent-shaped DFs (here they correspond to the upper and lower limits in y for the position of the particles shown in Figure 2c). First of all, in Figure 3, we observe a strong peak in E_y and B_z at the separatrix. Their values in the magnetosphere ($y < 25$) and in the selection region (between dashed lines) are negligible. The Hall electric field region is also where B_x becomes weaker, even if B_x remains at least twice as strong as B_z. E_x and E_z are negligible everywhere. The B_y component is more or less constant through the layer.

To model the phenomenon producing the crescent-shaped DFs, we simplify the separatrix layer as shown in Figure 4. In this model, we assume a Hall electric field layer along x, whose width is Δy along y and with constant E_y and B_z. The layer, the exhaust, and the magnetosphere also have a constant magnetic field B_x, as represented in Figure 4. We neglect the other field components. The particles in the layer are accelerated by the electric field and rotate around the magnetic field. Depending on the acceleration by the electric field and their incident angle when penetrating the layer, they will be able (or not) to cross the separatrix, as shown in the bottom of Figure 4.

Our model is based on one main assumption: The crescent shape in the DF is composed by magnetospheric cold ions crossing the Hall electric field layer in only one gyration. This can be verified in our model by solving the particle equations of motion, allowing us to deduce the particle energy gain during the crossing of the layer. The details of the calculations are given in the appendix, but they may be summarized as follows.

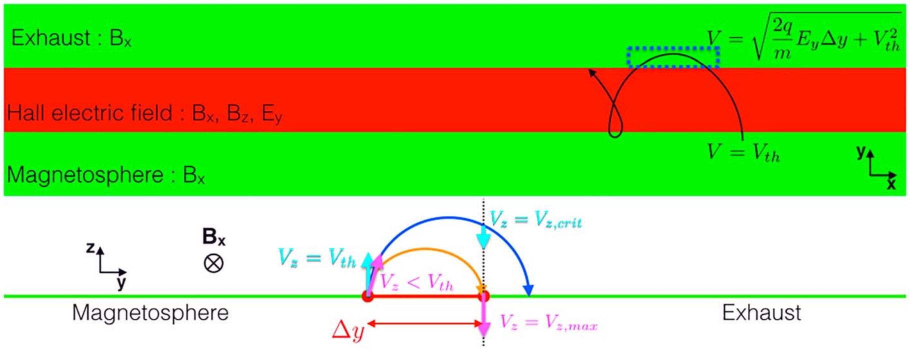

Figure 4. Schematic representation of the Hall electric field layer. The layer, in red and with a Δy width, is characterized by uniform B_z and E_y. A uniform B_x is present everywhere, including the magnetosphere and the exhaust, in green. The black arrow shows a cold ion trajectory. The norm of the particle velocity, as calculated by the model, is shown in the magnetosphere and in the exhaust. The dashed blue square shows a typical location where selected particles will produce a crescent-shaped distribution function. The bottom represents a cut of the layer in the (y, z) axis, with representation of two particle orbits through the layer. These orbits are made to represent the extremum orbits of the particles of the crescent (more details into the main text).

We consider the equation for the work of conservative forces,

$$\Delta E_c = \sum W, \tag{6}$$

where E_c is the kinetic energy and W the work made by the forces. Here the only working force is the electric field, so this equation can be rewritten as

$$\frac{1}{2}m(v^2 - v_{th}^2) = \int q\mathbf{E} \cdot d\mathbf{l} = qE_y\Delta y, \tag{7}$$

where m and q are the particle mass and charge, respectively; v its velocity; and v_{th} the thermal velocity of cold ions in the magnetosphere. Given that cold ions in the magnetosphere have for a typical velocity $v \in [0, v_{th}]$, we expect from equation (7) that any ion in the DF has

$$v < \sqrt{\frac{2q}{m}E_y\Delta y + v_{th}^2}. \tag{8}$$

In Figure 2c, we see that the crescent does not correspond to a complete half circle. As shown in Figure 4, the cold ion particles cross the Hall electric field layer in one gyration. Consequently, when a cold ion reaches the exhaust (and more specifically the region where we observe the signature), it has already performed part of its gyration around B_x. Thus, we can determine a minimum and a maximum velocity that cold ions can locally have along v_z. To find a local value of the velocity, we need to link the cold ion velocity v_z with its position y. We can express the position in y of a particle (details of calculation in the appendix) as

$$y(t) = A(\sin(\omega_c t + \Phi) - \sin(\Phi)) + y_0, \tag{9}$$

where A and Φ are constants that depend on the electromagnetic field. ω_c is the particle gyrofrequency. y_0 is the initial position of the particle, and we consider that at $t = 0$, the particle is crossing the boundary between the magnetosphere and the Hall electric field region. We can determine v_z:

$$v_z(t) = -\frac{q}{m}B_x A[\sin(\omega_c t + \Phi) - \sin(\Phi)] + v_{z,0} \tag{10}$$

$$= -\frac{q}{m}B_x[y(t) - y(0)] + v_{z,0}, \tag{11}$$

Now, we define $t = t_1$ the instant when the particle reaches the exhaust. Thus, we have $\Delta y = y(t_1) - y(0)$, where Δy is the width of the Hall field layer. There, the velocity $v_z(t_1) = v_{z,out}$ of a cold ion can therefore be written as

$$v_{z,out} = -\frac{q}{m}B_x\Delta y + v_{z,0}, \tag{12}$$

where $v_{z,0}$ is the velocity along z of the particle entering into the Hall field from the magnetosphere. Given v_{th} the thermal velocity of cold ions in the magnetosphere, a large majority of particles has $v_{z,0} \in [-v_{th}, v_{th}]$. The direction of rotation for cold ions coming from the magnetosphere to the exhaust only depends on the B_x direction. Consequently, once a cold ion enters the exhaust, its velocity is progressively transferred from $|v_y|$ to $|v_z|$. The minimum value of $|v_z|$ is therefore reached when the particle goes in or out of the exhaust. Thus, there exists a critical velocity $v_{z,crit}$ such that no particle from the crescent distribution can have $|v_z| < |v_{z,crit}|$, with

$$v_{z,crit} = -\frac{q}{m}B_x\Delta y + v_{th}. \tag{13}$$

This $v_{z,crit}$ is represented in Figure 4 with a white dashed line. Note that frozen-in particles drifting through the separatrix can also have a $v_{z,crit}$ velocity once they exit the layer. Thus, $|v_z| > |v_{z,crit}|$ is a necessary condition for particles forming the crescent.

On the other hand, the maximum value of v_z can be obtained from the maximum kinetic energy that a particle can have in the velocity plane perpendicular to the magnetic field once it crosses the layer. This

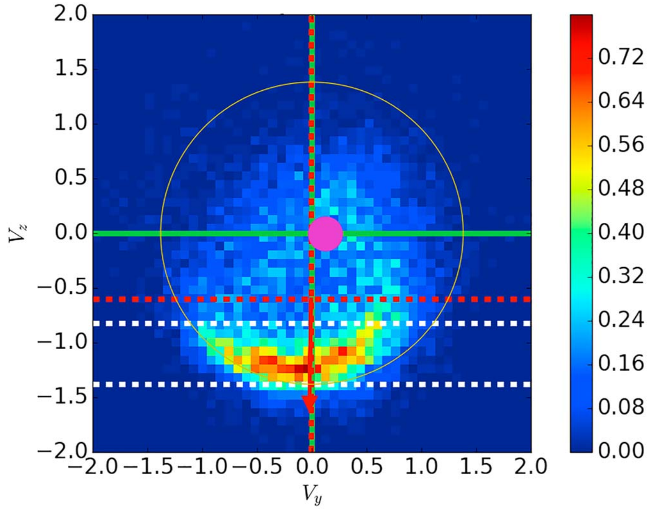

Figure 5. Same distribution function as in Figure 2c. Pointed red lines give the mean velocity of the distribution. The red arrow gives the direction of the mean velocity. The purple circle shows the $\mathbf{E} \times \mathbf{B}$ drift velocity. The yellow circle represents the theoretical value of the energy of ions from the crescent. It is calculated as a circle with a center $\mathbf{v} = \mathbf{0}$ and a radius $\sqrt{v^2 - v_x^2}$, where v is the norm of the velocity as calculated by the model and v_x the mean velocity along x of the particles in the distribution. The horizontal white dashed lines represent the minimum and maximum values of the crescent along v_z, as determined by the model.

scenario corresponds to particles that locally have all their perpendicular velocity along z, that is, $|v_{z,max}| = \sqrt{v_{max}^2 - v_x^2}$ (see bottom of Figure 4). The v_x (determined in appendix) can be written as follows:

$$v_x(t) = \frac{q}{m} B_z A[\sin(\omega_c t + \Phi) - \sin(\Phi)] + v_{x,0} \tag{14}$$

$$= \frac{q}{m} B_z [y(t) - y(0)] + v_{x,0}. \tag{15}$$

Thus, at the exit of the Hall field layer, we get

$$v_{x,out} = \frac{q}{m} B_z \Delta y + v_{x,0}, \tag{16}$$

with $v_{x,0} \in (-v_{th}, v_{th})$. In the model, $B_z = 0$ in the exhaust, so $v_{x,out}$ remains a constant, and we can thus write from equations (7) and (16):

$$|v_{z,max}| = \sqrt{v_{max}^2 - v_{x,out}^2} = \sqrt{\frac{2q}{m} E_y \Delta y + v_{th}^2 - v_{x,out}^2}. \tag{17}$$

Thanks to the equations (8) (v_{max}), (13) ($v_{z,crit}$), and (17) ($v_{z,max}$), we now have the characteristics of the crescent DF.

To check the model, we first have to determine the variables of the model (Δy, v_{th}, B_x, E_y, and ω_c). Δy is defined as the full width at half maximum of the peak of electric field, while E_y and B_z (included into ω_c) are defined as the maximum of their respective peaks. To determine those values, we used the smoothed values of electromagnetic fields, as done in Figure 3. For B_x and B_y, we used their mean value through the layer (not smoothed). $v_{th} = 0.3$ is calculated from the asymptotic cold ion temperature. Figure 5 shows a DF along with predictions from the model. The energy of the crescent ($mv^2/2$, calculated from equation (7)) is represented as a yellow circle. We note that the model prediction matches quite well with the DF. We also plotted the minimum and maximum values of $v_{z,out}$ (i.e., $v_{z,crit}$ and $v_{z,max}$) as dashed white lines. In Figure 5, we observe once again that the crescent is located in between the two v_z predicted by our model. This model thus appears to be a good description of the phenomenon behind the crescent-shaped signature.

Figure 2 shows that the crescent-shaped signature gradually disappears as one moves away from the X line. According to our model, this means that no cold ions are able to cross the layer in less than one gyration. We now use this model to determine an existence criteria for the crescent-shaped DF. A key point of this model is that the thermal velocity of cold ions is too small to let them cross the Hall electric field by thermal inertia. It is the normal electric field that allows cold ions to cross the layer by accelerating particles. The electric field action is opposed by the magnetic field, which forces particles to turn back. The existence criteria of the crescent signature mainly depends on the magnitude ratio between electric and magnetic fields and the width of the layer.

First of all, a particle is able to cross the layer if at any moment of its trajectory its location along y is located in the exhaust, in other words, if

$$\Delta y < max[y(t)] - y_0, \tag{18}$$

where y_0 the initial position of the particle (previously defined as located at the boundary between the magnetosphere and the Hall electric field layer), Δy the width of the layer, and $y(t)$ the particle position, as defined by equation (9). In order to determine an existence criteria, we need to solve equation (18) (see the appendix) and get

$$\Delta y < \frac{1}{\omega_c} \sqrt{v_{y,0}^2 + \frac{(E_y + B_x v_{0,z} - B_z v_{0,x})^2}{B_x^2 + B_z^2}} + \frac{1}{\omega_c^2} \frac{q}{m} (E_y + v_{z,0} B_x - v_{x,0} B_z). \tag{19}$$

As already stated, the crescent exists if particles can cross the layer. The existence criteria can thus be determined by maximizing the right-hand term of equation (19). The optimal orientation of the initial velocity to

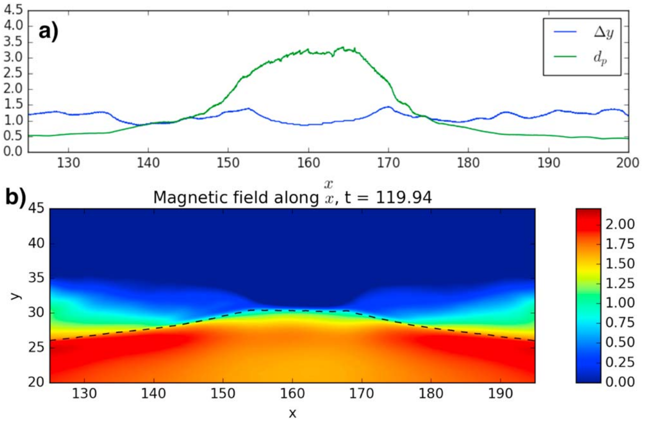

Figure 6. (a) Width Δy of the Hall electric field layer and penetration length d_p along the separatrices. Results are plotted along the x axis. (b) Magnetic field along x (only when positive). The black dashed line represents the separatrices and is calculated as the maximum of E_y along y.

cross the layer is $\mathbf{v}_0 = v_{th}\mathbf{e}_z$, given that $B_x > B_z$ (see Figure 4). As a result, we determine from equation (19) that there exist particles crossing the layer if

$$\Delta y < \frac{2q}{m\omega_c^2}(E_y + B_x v_{th}) = d_p, \tag{20}$$

where d_p is the penetration length of the particle inside of the layer.

To check the validity of equation (20), we calculate Δy and d_p by taking the characteristic values of the fields in the simulation along the magnetospheric separatrices. In Figure 6a we plot Δy and d_p along x at the magnetospheric separatrices. We observe that equation (20) is satisfied only between $x \approx 138$ and $x \approx 175$. In Figure 6b, we can see the magnetic field along x together with the position of the magnetospheric separatrices. As we move further away from the X line ($x \approx 165$) and despite of a kind of plateau corresponding to the electron diffusion region, d_p decreases. This is partly a consequence of the decrease of the Hall electric field and partly because of the increase of the magnetic field as we move away from the X line along the separatrix (in our case, the increase of **B** is much more important than the decrease of **E**). The width of the Hall electric field region, on the other hand, is more or less constant. If we look at the presence or the absence of crescent-shaped DFs along the separatrices (see Figure 2), we observe that crescents are located along the layer between $x \approx 138$ and $x \approx 180$, except where the cold ion density is very low. The existence criteria (equation (20)) is thus quite well satisfied, considering the simplification made in the model. However, despite the criteria being satisfied, we do not observe crescents between $x \approx 150$ and $x \approx 170$, because of the drop in the cold ion density, as discussed in section 3.1.

Particles which are unable to cross the Hall electric field region in less than one gyration will nevertheless cross the separatrix by $\mathbf{E} \times \mathbf{B}$ drifting within the main magnetic field B_x and the reconnection electric field E_z, but this process is much slower, and these particles will also $\mathbf{E} \times \mathbf{B}$ drift along x (direction of the exhaust velocity) because of the Hall fields (B_z and E_y). As a result, these particles are not observed in the exhaust near the X line. To summarize, when those particles cross the Hall fields they will not have crescent-shaped DFs but gyrotropic DFs with possibly other deformations associated with the presence of strong gradients. Those DFs are typically observed further away from the X line where cold ions are frozen-in and will be discussed in section 3.3. The dynamics behind the crescent-shaped signature is not specific to cold ions, but the crescent appears because $mv_{th}^2/2 << qE_y\Delta y$. In other words, for other ion populations with higher v_{th} no crescent structure can develop because the potential jump is negligible compared to the particle energy.

3.3. Comparison of Ion DFs for Different Populations and Cold Ion Parallel Heating

At the magnetopause, cold ions have different dynamics as compared to other ions mainly because they are frozen-in while the other ion populations are not. In this subsection, we are interested in the relative modifications of the ion population distribution functions (DFs) occurring near the magnetospheric separatrix where all ions are present. In Figure 7, we show the particle DFs of the ion populations taken along a cold ion streamline. The streamline is shown in Figure 2a together with the locations where the particles of the distributions are picked (blue squares).

The first row of the DFs shows that of cold ions. As a very low-energy population, cold ions are frozen in to the magnetic field as long as they remain in the magnetosphere (Figure 7g) where their DFs are isotropic. Once in the current layer, cold ions deviate from the $\mathbf{E} \times \mathbf{B}$ drift velocity (purple point in Figure 7d). They are accelerated along x leading to a deformation of the DF in that direction. We observe, however, that v_x becomes larger than the $\mathbf{E} \times \mathbf{B}$ drift velocity (purple point in Figure 7d, which has here an x component because of the Hall fields E_y and B_z) and the DF deforms itself in that direction. This means an acceleration unrelated to the $\mathbf{E} \times \mathbf{B}$ drift, which leads to a temperature anisotropy with $T_{xx} > T_{yy}, T_{zz}$. Note that the magnetic field is mainly oriented along x, so that $T_{xx} \approx T_{//}$. Once fully within the Hall electric field region (see Figure 7a), the temperature is isotropic once again. This means that cold ions crossing the separatrix are first heated in the parallel direction and then get heated in the perpendicular direction.

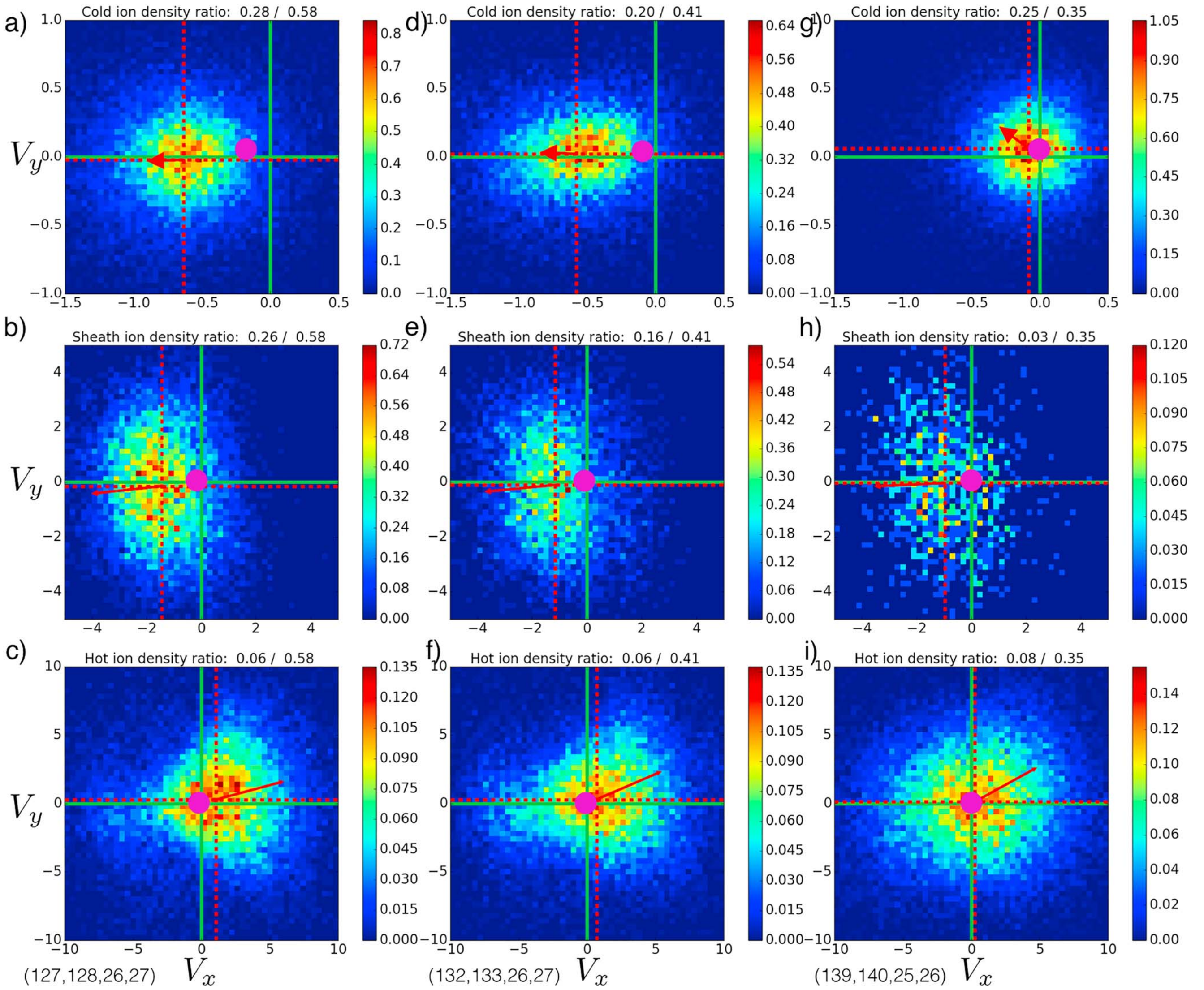

Figure 7. Ion distribution functions in the (v_x, v_y) plane for three different ion populations near the magnetospheric separatrix. Each line corresponds to an ion population: cold magnetospheric ion (distributions a, d, and g), magnetosheath ions (distributions b ,e, and h), and hot magnetospheric ions (distributions c, f, and i). Each column corresponds to a different location, picked along a same cold ion streamline crossing the Hall electric field. These locations are plotted in blue in Figure 2a: left blue square for distributions (a–c), central blue square for distributions (d–f), and right blue square for distributions (g–i). $(x_{min}, x_{max}, y_{min}, y_{max})$ coordinates of each blue square are given at the bottom of the column. The distributions are made by integration long the v_z axis. Dashed red lines give the mean velocity of the distribution, that is, for the plotted population. The red arrow gives the direction of the velocity. The purple circle shows the $\mathbf{E} \times \mathbf{B}$ drift velocity.

The second row of DFs in Figure 7 shows magnetosheath ions. Despite the distributions being picked at the magnetosphere side of the exhaust, the density of magnetosheath ions is locally of the same the order of magnitude as that of the cold ions (Figures 7a and 7d). As expected, the more we look into the magnetosphere (Figure 7h), the more their density decreases. Magnetosheath ions are also more energetic than cold ions ($T_{ish}/T_{ic} \sim 100$). We indeed observe that their standard deviation along v_y is way larger than that of cold ions. Their DFs, as for cold ions, are shifted in the negative v_x direction and take a D shape, which is a typical signature of magnetosheath ions in the exhaust near the magnetospheric separatrix (Cowley, 1982). Such D-shaped distributions appear there because at the magnetospheric separatrix the magnetic field lines are linked on one side to the magnetosphere, devoid of magnetosheath ions, and on the other side to the exhaust, from which magnetosheath ions flow. The consequence is that the velocities of cold magnetospheric ions and magnetosheath ions are orientated in the same direction.

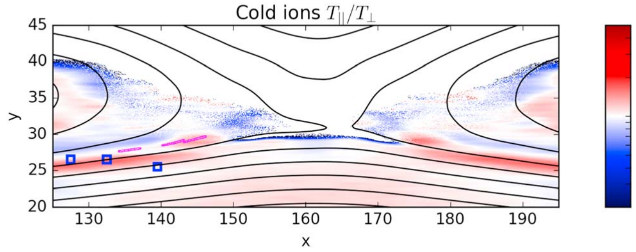

Figure 8. Ratio of parallel over perpendicular cold ion temperatures. Black lines represent magnetic field lines. The color palette shows this ratio only when the cold ion density is higher than 0.02 n_0. The purple (blue) contours show the positions of particle distributions shown in Figure 2 (Figure 7).

The third row in Figure 7 shows the hot magnetospheric ions DFs. These ions are much more energetic than cold ions ($T_{ih}/T_{ic} \sim 500$). Due to their high temperatures, their DFs are impacted by Larmor radius effects over a broader area with respect to the other populations. Indeed, the DFs of hot ions are not isotropic even for the ones sampled in the magnetosphere (Figure 7i). The other specificity of hot magnetospheric ions is their bulk velocity. Unlike cold magnetospheric ions and magnetosheath ions, the hot ions have a positive mean v_x. This behavior has been already observed by Gosling et al. (1990) in the context of flux transfer events. In this case, the counter-streaming ions are the magnetospheric ring current ions leaking out of the magnetosphere along the reconnected magnetic field lines. This phenomenon is probably similar here, but this is beyond the scope of this paper. However, we are interested in these DFs in order to confirm that hot magnetospheric ions can easily be discriminated from cold magnetospheric ions when observing the full ion DF thanks to their high energy.

We have observed that the cold ion DFs (first row of Figure 7) are anisotropic along the magnetospheric separatrices where they are heated in the direction parallel to the magnetic field. In Figure 8, we see the ratio of parallel over perpendicular cold ion temperatures. We observe that the cold ion temperature is mainly parallel (i.e., in red) along the magnetospheric separatrices. An exception is around the diffusion region where instead they are mostly heated in the perpendicular direction (in blue), but we already show in section 3.1 that both the density and the dynamics of cold ions are different there. In the magnetosphere (i.e., below the Hall electric field region), cold ions are nearly isotropic. Their temperature has a slight parallel anisotropy for $x \in [130, 190]$ and a slight perpendicular anisotropy for $x > 190$ and $x < 130$. These small anisotropies result from the conservation of particle's mean magnetic moment given by $< \mu > = k_B T_{\perp}/B$ (Baumjohann & Treumann, 1997), where k_B the Boltzmann constant, B the norm of the magnetic field, and $T_{\perp}$ the population temperature in the direction perpendicular to the magnetic field. We start by noticing that the magnetic field decreases more and more as we get within the diffusion region (see Figure 6b). There (i.e., for $x \in [130, 190]$ in the magnetosphere), in order to conserve the magnetic moment, $T_{\perp}$ decrease while $T_{//}$ remains constant. By contrast, further away from the reconnection region (i.e., for $x > 190$ and $x < 130$ in the magnetosphere), the pileup of magnetic field lines along the separatrices causes a magnetic field increase, and thus, $T_{\perp}$ also increases. In the exhaust, that is, for y above the separatrices, cold ions have a higher perpendicular temperature, except in the core of the exhaust where the plasma has never been involved in the reconnection dynamics. There, the temperature is mainly parallel, but given the very low density of cold ions there ($n_{ic} < 0.04$), the measurement relevance is questionable (less than 7 cold ion macroparticles per simulation cell). However, because of the exhaust dynamics, this plasma does not impact the dynamics at the separatrices and therefore has no impact on the discussions of this article. We consider that the magnetospheric separatrices are the only region where cold ions have both an anisotropic temperature and a nonnegligible density. On the other hand, we know from section 3.1 that most of the cold ions enter the exhaust by crossing these separatrices. Therefore, how does parallel heating occur as cold ions enter the exhaust? This question is still unanswered, but we present here some clues.

The observation in our simulation of a parallel heating of cold ions along magnetospheric separatrices is unexpected, as observational studies of cold ions show a perpendicular heating of cold ions in the Hall electric field region (Graham et al., 2017; Toledo-Redondo, André, Vaivads, et al., 2016). However, we observed that the parallel heating of cold ions begins before they reach this region. In Figure 9a, we plot the different diagonal components of the cold ion temperature tensor. We observe for $y \sim 24$ that the parallel temperature starts to rise up, while the perpendicular components remain unchanged and begin to increase at $y \sim 26$ once we reach the Hall electric field region. Their growth is quicker than the parallel one. At $y \sim 27$ the temperature becomes more perpendicular than parallel. There may be several possible explanations for the heating observed for $26 < y < 27.5$ in the Hall electric field region. In particular, the presence of a parallel ambipolar electric field (Scudder et al., 2002) could explain the parallel heating, and an electric field gradient perpendicular to the magnetic field may provide an efficient mechanism for perpendicular heating (Cole, 1976; Toledo-Redondo, André, Vaivads, et al., 2016). We now focus on what happens at $24 < y < 26$. Figure 9b shows the parallel velocity of cold ions together with its projection on v_x, v_y, and v_z. We observe that for the region of interest the parallel velocity is more or less superposed with the velocity along x. We

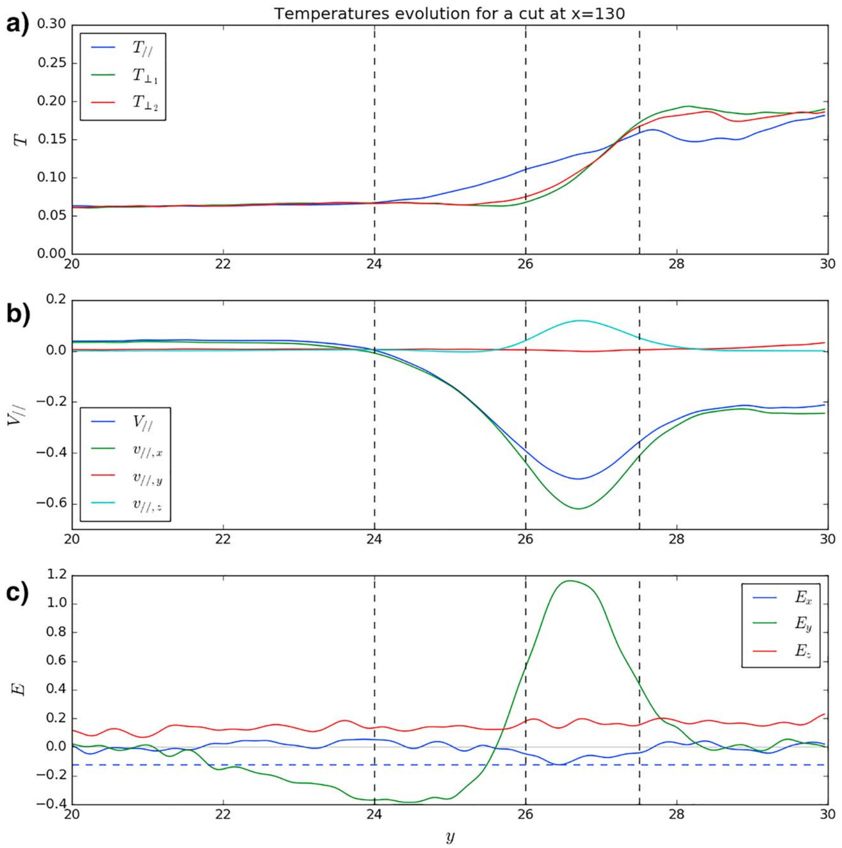

Figure 9. Components of the cold ion temperature, cold ion parallel velocity, and electric field for a cut at $x = 130$ and $t = 120$. (a) Diagonal components of the temperature tensor in the $(//, \perp_1, \perp_2)$ frame. (b) Mean velocity of cold ions in the direction parallel to the magnetic field and its projection upon x, y, and z directions. (c) Electric field components. A dashed blue line show the minimum value of E_x. Vertical dashed lines are plotted for $y = 24$, 26, and 27.5 in order to roughly show the area where the heating is only parallel (for $24 < y < 26$) and the position of the Hall electric field peak (for $26 < y < 27.5$).

also observe on this plot that for $24 < y < 26$, $v_{//}$ decreases from zero toward a negative peak: Cold ion streamlines begin to turn (see Figure 1). In Figure 9c we plot the electric field components along the cut. We see the positive peak of E_y corresponding to the Hall electric field and a small peak of the x component of the electric field ($E_x \sim -0.1$). The small E_x layer probably corresponds to the ambipolar electric field (Scudder et al., 2002), but its low amplitude, relative to the noise of the simulation, makes the study of its potential relation with the parallel heating challenging.

In Figure 9, we observe that the cold ions begin to accelerate in the parallel direction before reaching the Hall electric field region. This particle acceleration results in a parallel heating, as particles at a given location are faster owing to their gyrocenter being located deeper into the acceleration layer. However, the origin of this acceleration not well understood for now. Therefore, future work shall be performed to understand the mechanism behind the cold ion parallel heating along magnetospheric separatrices.

4. Discussions

In this work, we used numerical simulations to highlight three signatures specific to magnetospheric cold ions in the vicinity of an asymmetric reconnecting boundary representative of the dayside Earth's magnetopause. The first signature is that of a rarefaction of cold ions near the diffusion region, along with a related compression along the magnetospheric separatrices. The second signature is a crescent-shaped DF in the velocity space plane perpendicular to the magnetic field. This signature is observable along magnetospheric separatrices in the near exhaust. The third signature is a cold ion heating parallel to the magnetic field along the separatrices. The crescent-shaped DF looks like previously reported ion and electron signatures (Hesse et al., 2014; Shay et al., 2016; Wang et al., 2016), despite a different mechanism. In the later papers, this signature results of a magnetic field reversal, while in our case it comes from the Hall electric field acceleration.

The rarefaction of cold ions at the X line observed in our simulation can be of use as a signature of magnetic reconnection in the presence of cold ions. It is however doubtful that this signature will be identified in observations, given the difficulty to distinguish cold ions from the others at the magnetopause (Toledo-Redondo, André, Khotyaintsev, et al.,2016). By contrast, the compression of cold ions along magnetospheric separatrices may have an impact on the plasma dynamics at the magnetopause. Indeed, even if cold ions are scarce in the magnetosphere, their density rises at the magnetopause, and thus, their role should not be neglected. Their local effects, for example, on the Hall electric field, will be reinforced (André et al., 2016; Dargent et al., 2017; Toledo-Redondo et al., 2015, 2018).

Crescent-shaped DFs have recently drawn a lot of attention as a signature of magnetic reconnection sites. Predicted by simulation in Hesse et al. (2014), crescent-shaped electron distributions were used to identify electron diffusion regions in MMS data (Burch et al., 2016). The origin of this signature have been studied a lot (Bessho et al., 2016; Egedal et al., 2016; Lapenta et al., 2017; Zenitani et al., 2017). This signature results from Speiser (1965) orbits. In the context of magnetic reconnection, Speiser orbits are restrained to the diffusion region and the center of the exhaust, which are the only places where antiparallel magnetic field lines are observed over scales comparable to the gyroradius of the particles. This result has been generalized to ions (Dargent et al., 2017; Shay et al., 2016), whose U-turn in the magnetosphere also produces a crescent-shaped signature. Wang et al. (2016) also showed that this signature can split into two crescents near the Hall electric field, which acts like a filter for low-energy particles. Two crescents are locally formed there: one for ions able to cross the electric field and one for the reflected ions. The common point between all those signatures is that they result from Speiser-type orbits and therefore need a magnetic field reversal at the scales of the population mean Larmor radius. Their formation mechanism therefore differs from the one presented in this work. The idea that short-width electric field can produce crescent-shaped DF had was already presented by Price et al. (2016). This idea is developed by Egedal et al. (2016), whose model explains how crescent-shaped DFs of electrons can appear, even without Speiser orbits. This model is probably the nearest to the model described in this article. However, because of the differences of scale and temperature between electrons and cold ions, some specificities exist between the models, especially on the assumptions on electromagnetic fields. In particular, we take into account the Hall magnetic field (B_z), which can be strong enough to impact the gyration of ions at the separatrix.

The various signatures presented in this work share a common feature: They are located along or adjacent to magnetospheric separatrices. Knowing that a separatrix region crossing lasts few seconds to few tens of seconds (André et al., 2016; Khotyaintsev et al., 2006; Toledo-Redondo et al., 2017), the FPI instruments onboard MMS (Pollock et al., 2016) are currently the only instruments able to observe such fine details, thanks to a time resolution of 150 ms for ions. The temperature of the cold ions is usually close to the lower energy limit of the FPI instrument, which is in turn close to the usual ion drift energies near the magnetopause, owing to the relative motion between the spacecraft and the ambient plasma. Nevertheless, FPI should be able to resolve these crescents at least for some favorable cases (cold ion temperatures of several tens of eV to few hundred eV and drift energies of no more than 10-20 eV). While ion crescents such as those described in Shay et al. (2016) have already been observed (Wang et al., 2016), the cold ion crescents reported here remain to be found in MMS data.

The signatures described here are of particular interest to understand how low-energy ion heating occurs along the separatrices. At present, two mechanisms are cited to explain cold ion heating along separatrices: waves and large electric field gradients (Toledo-Redondo, André, Vaivads, et al.,2016; Toledo-Redondo et al., 2017). The heating by electromagnetic waves happens for instance when their frequency is close to the ion cyclotron frequency (André et al., 1994; Chang et al., 1986; Graham et al., 2017). However, the relatively small size of our simulations and the heavy electrons (mass ratio of 25) hinder the development of waves, and thus, this process cannot be studied. The Hall electric field effect is the important driver in our simulation. Cole (1976) proposed a model for ion heating by a strong electric field gradient, perpendicular to the magnetic field. From his model, we expect a perpendicular heating from our observed Hall electric field along the separatrix. The model of Cole (1976) has recently been used to explain the perpendicular heating of cold ions observed in MMS data (Toledo-Redondo, André, Vaivads, et al.,2016), as well as in symmetrical simulations (Divin et al., 2016). The cold ion parallel heating observed in our simulation implies that there may exist another process capable of heating cold ions (though, again, this time in the direction parallel to the magnetic field). In our simulation, this process is more efficient than the perpendicular heating. The comprehension of this mechanism and its relative importance compared to others (e.g., waves) require future-dedicated work using both spacecraft data and simulations. We note that this temperature anisotropy ($T_{//}/T_{\perp} \sim 2$) is small but not negligible compared to the perpendicular heating observed along the separatrices by Divin et al. (2016) ($T_{//}/T_{\perp} \sim 0.1$) and Toledo-Redondo et al. (2017) ($T_{//}/T_{\perp} \sim 0.3$).

5. Conclusion

In this paper, we have highlighted and analyzed several key signatures of magnetospheric cold ions using a fully kinetic 2-D simulation of a typical dayside magnetopause undergoing magnetic reconnection. We showed that consistent with a fluid behavior, the divergence of cold ion streamlines on either side of the reconnection site causes a local rarefaction of cold ions very near the magnetic X line. By contrast, streamlines converge at the magnetospheric separatrices and so that cold ion density is enhanced by compression there. We also identified an interesting signature of cold ions at the separatrix: Their DF in the velocity space plane perpendicular to the magnetic field can be crescent shaped. We built a theoretical model that explains this signature very well, using a combination of a strong cold ion density gradient and a strong normal electric field (the Hall electric field). In this model, the crescent-shaped signatures appear when cold ions can cross the electric field layer in less than one gyration and reach the side with few cold ions. We also defined an existence criteria for this signature, which should ease its observation in spacecraft data. Indeed, if cold ions cannot cross the electric field in less than one gyration, there is no signature. Then, we compared the DFs of each ion populations near the separatrix. In doing so, we noticed a parallel heating of cold ions in this region, which remains to be fully explained.

Cold ions often have an important contribution to the total magnetospheric ion density. They thus have a significant impact on magnetic reconnection, especially regarding energy partitioning in the process (Toledo-Redondo et al., 2017). However, observational studies of their partitioning remain hard to perform because the heating of the cold ion population makes them more difficult to distinguish from other ions in spacecraft measurement. In that respect, simulations thus remain a key, complementary tool for performing such work in the future.

Appendix A

The simplified model of the Hall electric field showed in Figure 4 allows us to determine any particle trajectory in the current layer. Electromagnetic fields are deemed constant in the layer and defined as

$$\mathbf{B} = B_x\mathbf{e}_x + B_z\mathbf{e}_z, \tag{A1}$$

$$\mathbf{E} = E_y\mathbf{e}_y. \tag{A2}$$

Outside of the layer, we simply take

$$\mathbf{B} = B_x\mathbf{e}_x, \tag{A3}$$

$$\mathbf{E} = \mathbf{0}. \tag{A4}$$

Moreover, we consider that a particle entering the layer has a velocity $\mathbf{v}_0$, such as

$$\mathbf{v}_0 = v_{x,0}\mathbf{e}_x + v_{y,0}\mathbf{e}_y + v_{z,0}\mathbf{e}_z, \tag{A5}$$

$$v_0^2 = v_{x,0}^2 + v_{y,0}^2 + v_{z,0}^2 = v_{th}^2, \tag{A6}$$

where v_{th} is the cold ion thermal velocity in the magnetosphere. We put $t_0 = 0$ the time at which the particle enters the layer at the position $y = y_0$.

A1. Resolution of the Equations of Motion

First are the equations of motion:

$$\frac{m}{q}\frac{dv_x}{dt} = v_y B_z, \tag{A7}$$

$$\frac{m}{q}\frac{dv_y}{dt} = E_y + v_z B_x - v_x B_z, \tag{A8}$$

$$\frac{m}{q}\frac{dv_z}{dt} = -v_y B_x. \tag{A9}$$

Let us derive

$$\frac{d^2 v_x}{dt^2} = \frac{q}{m}\frac{dv_y}{dt}B_z, \tag{A10}$$

$$\frac{d^2 v_y}{dt^2} = -\omega_c^2 v_y, \tag{A11}$$

$$\frac{d^2 v_z}{dt^2} = -\frac{q}{m}\frac{dv_y}{dt}B_x. \tag{A12}$$

We deduce from equation (A11) the velocity along y and its derivative:

$$v_y = \omega_c A\cos(\omega_c t + \Phi), \tag{A13}$$

$$\frac{dv_y}{dt} = -\omega_c^2 A\sin(\omega_c t + \Phi), \tag{A14}$$

where Φ and A are constants that we will determine.

At $t = 0$, using the previous equations and equation (A8), we obtain

$$v_y(0) = \quad v_{y,0} \quad = \omega_c A\cos(\Phi), \tag{A15}$$

$$\frac{dv_y}{dt}(0) = \quad \frac{q}{m}(E_y + v_{z,0}B_x - v_{x,0}B_z) = \quad -\omega_c^2 A\sin(\Phi), \tag{A16}$$

and, from there,

$$\tan(\Phi) = -\frac{q}{m\omega_c v_{0,y}}(E_y + B_x v_{0,z} - B_z v_{0,x}), \tag{A17}$$

$$\omega_c^2 A^2 = v_{y,0}^2 + \frac{(E_y + B_x v_{0,z} - B_z v_{0,x})^2}{B_x^2 + B_z^2}. \tag{A18}$$

From equation (A14) and then equations (A7) and (A9), we can determine the velocity in all directions:

$$v_y = \omega_c A\cos(\omega_c t + \Phi), \tag{A19}$$

$$v_x = \frac{q}{m}B_z A[\sin(\omega_c t + \Phi) - \sin(\Phi)] + v_{x,0}, \tag{A20}$$

$$v_z = -\frac{q}{m}B_x A[\sin(\omega_c t + \Phi) - \sin(\Phi)] + v_{z,0}. \tag{A21}$$

A2. Calculation of the Kinetic Energy of Particles in the Crescent

The integration of the velocity equation gives us

$$y(t) = A(\sin(\omega_c t + \Phi) - \sin(\Phi)) + y_0. \tag{A22}$$

We set Δy the width along y of the Hall electric field layer. From equation (A22) and for t_1 the time at which the particle leaves the layer on the exhaust side, we have

$$\Delta y = y(t_1) - y(0) = A(\sin(\omega_c t_1 + \Phi) - \sin(\Phi)). \tag{A23}$$

Thanks to velocities and equations (A23), (A15), and (A16), we deduce the kinetic energy of a particle at the exit of the exhaust side of the layer. After some calculation, we obtain

$$E_c = \frac{1}{2}mv^2 = \frac{1}{2}mv_{th}^2 + q\Delta y E_y. \tag{A24}$$

With this method, calculation are heavy. We can find the same result using the conservation of forces, as done in section 3.2. We therefore obtain the same results as equation (7).

A3. Crescent Velocity Space Limits Along v_z

We now want to determine the minimum velocity along z in the crescent-shaped distributions. For that, we look at the exit of the layer on the exhaust side, and we substitute equation (A23) into equation (A21) at $t = t_1$. We deduce that v_z is equal to

$$v_z(t_1) = -\frac{q}{m}B_x \Delta y + v_{z,0}, \tag{A25}$$

with $v_{z,0} \in [-v_{th}, v_{th}]$.

A4. Crescent Distribution Existence Criterion

For the crescent-shaped distribution to appear, we need cold ions to cross the Hall electric field layer in less than one gyration. This means that there exists a moment of the trajectory at which the particle reach the exhaust, that is,

$$\Delta y < max[y(t)] - y_0, \tag{A26}$$

where y_0 the initial position of the particle (previously defined as located at the boundary between the magnetosphere and the Hall electric field layer), Δy the width of the layer and $y(t)$ the particle position, as defined by equation (A22).

From equation (A22) and by using equations (A18) and (A16), we can resolve the right-hand side of equation (A26):

$$max[y(t)] - y_0 = A(1 - sin(\Phi)) \tag{A27}$$

$$= \frac{1}{\omega_c}\omega_c A + \frac{1}{\omega_c^2}[-\omega_c^2 A sin(\Phi)] \tag{A28}$$

$$= \frac{1}{\omega_c}\sqrt{v_{y,0}^2 + \frac{(E_y + B_x v_{0,z} - B_z v_{0,x})^2}{B_x^2 + B_z^2}} + \frac{1}{\omega_c^2}\frac{q}{m}(E_y + v_{z,0}B_x - v_{x,0}B_z). \tag{A29}$$

We now want to determine if particles are able to cross the layer. For that, we have to define $\mathbf{v}_0$ in order to maximize equation (A29). In this case, we have to take $\mathbf{v}_0 = v_{th}\mathbf{e}_z$. With this value of $\mathbf{v}_0$, we determine from (A26) and (A29) that a particle is able to cross the layer if

$$\Delta y < \frac{2q}{m\omega_c^2}(E_y + B_x v_{th}). \tag{A30}$$

In practice, the cold ion thermal velocity is negligible, and we can assimilate the electric field along y to the total local electric field. This helps to simplify the criterion as

$$\Delta y < \frac{2q}{m\omega_c^2}E. \tag{A31}$$

Acknowledgments
The authors acknowledge the Agence National de la Recherche (ANR) for funding the project MON-ANR (ANR-13-PDOC-0027) supporting this research. Work at IRAP was performed with the support of CNRS and CNES. We also acknowledge the support of the ISSI's international teams *MMS and CLUSTER observations of magnetic reconnection* and *Cold plasma of ionospheric origin at the Earth's magnetosphere*. The authors thank the SMILEI development team. This work was granted access to the HPC resources of IDRIS under the allocation i2015047231. Sergio Toledo-Redondo acknowledges support of the Ministry of Economy and Competitiviness (MINECO) of Spain, research project FIS2017-90102-R. The source code of the simulation used in this paper is open-source and available at https://github.com/SmileiPIC/Smilei and http://www.maisondelasimulation.fr/smilei/index.html. The necessary informations for reproducing the simulation results discussed here are clearly written in the article.

References

André, M., & Cully, C. M. (2012). Low-energy ions: A previously hidden solar system particle population. *Geophysical Research Letters*, *39*, L03101. https://doi.org/10.1029/2011GL050242

André, M., Li, W., Toledo-Redondo, S., Khotyaintsev, Y. V., Vaivads, A., Graham, D. B., et al. (2016). Magnetic reconnection and modification of the hall physics due to cold ions at the magnetopause. *Geophysical Research Letters*, *43*, 6705–6712. https://doi.org/10.1002/2016GL069665

André, M., Norqvist, P., Vaivads, A., Eliasson, L., Norberg, O., Eriksson, A. I., & Holback, B. (1994). Transverse ion energization and wave emissions observed by the Freja satellite. *Geophysical Research Letters*, *21*(17), 1915–1918. https://doi.org/10.1029/94GL00699

André, M., Vaivads, A., Khotyaintsev, Y. V., Laitinen, T., Nilsson, H., Stenberg, G., et al. (2010). Magnetic reconnection and cold plasma at the magnetopause. *Geophysical Research Letters*, *37*, L22108. https://doi.org/10.1029/2010GL044611

Aunai, N., Belmont, G., & Smets, R. (2011). Energy budgets in collisionless magnetic reconnection: Ion heating and bulk acceleration. *Physics of Plasmas*, *18*(12), 122901. https://doi.org/10.1063/1.3664320

Baumjohann, W., & Treumann, R. A. (1997). *Basic space plasma physics*. London: Imperial College Press.

Bessho, N., Chen, L.-J., & Hesse, M. (2016). Electron distribution functions in the diffusion region of asymmetric magnetic reconnection. *Geophysical Research Letters*, *43*, 1828–1836. https://doi.org/10.1002/2016GL067886

Borovsky, J. E., & Denton, M. H. (2006). Effect of plasmaspheric drainage plumes on solar-wind/magnetosphere coupling. *Geophysical Research Letters*, *33*, L20101. https://doi.org/10.1029/2006GL026519

Burch, J. L., Torbert, R. B., Phan, T. D., Chen, L.-J., Moore, T. E., Ergun, R. E., et al. (2016). Electron-scale measurements of magnetic reconnection in space. *Science*, *352*, 6290. https://doi.org/10.1126/science.aaf2939

Cassak, P. A., & Shay, M. A. (2007). Scaling of asymmetric magnetic reconnection: General theory and collisional simulations. *Physics of Plasmas*, *14*(10), 102114. https://doi.org/10.1063/1.2795630

Chang, T., Crew, G. B., Hershkowitz, N., Jasperse, J. R., Retterer, J. M., & Winningham, J. D. (1986). Transverse acceleration of oxygen ions by electromagnetic ion cyclotron resonance with broad band left-hand polarized waves. *Geophysical Research Letters*, *13*(7), 636–639. https://doi.org/10.1029/GL013i007p00636

Cole, K. D. (1976). Effects of crossed magnetic and (spatially dependent) electric fields on charged particle motion. *Planetary and Space Science*, *24*(5), 515–518. https://doi.org/10.1016/0032-0633(76)90096-9

Cowley, S. W. H. (1982). The causes of convection in the Earth's magnetosphere: A review of developments during the IMS. *Reviews of Geophysics*, *20*(3), 531–565. https://doi.org/10.1029/RG020i003p00531

Dargent, J., Aunai, N., Lavraud, B., Toledo-Redondo, S., Shay, M. A., Cassak, P. A., & Malakit, K. (2017). Kinetic simulation of asymmetric magnetic reconnection with cold ions. *Journal of Geophysical Research: Space Physics*, *122*, 5290–5306. https://doi.org/10.1002/2016JA023831

Derouillat, J., Beck, A., Pérez, F., Vinci, T., Chiaramello, M., Grassi, A., et al. (2017). Smilei : A collaborative, open-source, multi-purpose particle-in-cell code for plasma simulation. *Computer Physics Communications*, *222*, 351–373. https://doi.org/10.1016/j.cpc.2017.09.024

Divin, A., Khotyaintsev, Yu. V., Vaivads, A., André, M., Toledo-Redondo, S., Markidis, S., & Lapenta, G. (2016). Three-scale structure of diffusion region in the presence of cold ions. *Journal of Geophysical Research: Space Physics*, *121*, 12,001–12,013. https://doi.org/10.1002/2016JA023606

Egedal, J., Le, A., Daughton, W., Wetherton, B., Cassak, P. A., Chen, L.-J, et al. (2016). Spacecraft observations and analytic theory of crescent-shaped electron distributions in asymmetric magnetic reconnection. *Physical Review Letters*, *117*, 185101. https://doi.org/10.1103/PhysRevLett.117.185101

Fuselier, S. A., Burch, J. L., Cassak, P. A., Goldstein, J., Gomez, R. G., Goodrich, K., et al. (2016). Magnetospheric ion influence on magnetic reconnection at the duskside magnetopause. *Geophysical Research Letters*, *43*, 1435–1442. https://doi.org/10.1002/2015GL067358

Gosling, J. T., Thomsen, M. F., Bame, S. J., Elphic, R. C., & Russell, C. T. (1990). Plasma flow reversals at the dayside magnetopause and the origin of asymmetric polar cap convection. *Journal of Geophysical Research*, *95*(A6), 8073–8084. https://doi.org/10.1029/JA095iA06p08073

Graham, D. B., Khotyaintsev, Y. V., Norgren, C., Vaivads, A., André, M., Toledo-Redondo, S., et al. (2017). Lower hybrid waves in the ion diffusion and magnetospheric inflow regions. *Journal of Geophysical Research: Space Physics*, *122*, 517–533. https://doi.org/10.1002/2016JA023572

Hesse, M., Aunai, N., Sibeck, D., & Birn, J. (2014). On the electron diffusion region in planar, asymmetric, systems. *Geophysical Research Letter*, *41*, 8673–8680. https://doi.org/10.1002/2014GL061586

Khotyaintsev, Y. V., Vaivads, A., Retinò, A., André, M., Owen, C. J., & Nilsson, H. (2006). Formation of inner structure of a reconnection separatrix region. *Physical Review Letters*, *97*, 205003. https://doi.org/10.1103/PhysRevLett.97.205003

Lapenta, G., Berchem, J., Zhou, M., Walker, R. J., El-Alaoui, M., Goldstein, M. L., et al. (2017). On the origin of the crescent-shaped distributions observed by mms at the magnetopause. *Journal of Geophysical Research: Space Physics*, *122*, 2024–2039. https://doi.org/10.1002/2016JA023290

Lavraud, B., & Larson, D. E. (2016). Correcting moments of in situ particle distribution functions for spacecraft electrostatic charging. *Journal of Geophysical Research: Space Physics*, *121*, 8462–8474. https://doi.org/10.1002/2016JA022591

Li, W. Y., André, M., Khotyaintsev, Y. V., Vaivads, A., Fuselier, S. A., Graham, D. B., et al. (2017). Cold ionospheric ions in the magnetic reconnection outflow region. *Journal of Geophysical Research: Space Physics*, *122*, 10,194–10,202. https://doi.org/10.1002/2017JA024287

McFadden, J. P., Carlson, C. W., Larson, D., Bonnell, J., Mozer, F. S., Angelopoulos, V., et al. (2008). Structure of plasmaspheric plumes and their participation in magnetopause reconnection: First results from themis. *Geophysical Research Letters*, *35*, L17S10. https://doi.org/10.1029/2008GL033677

Pollock, C., Moore, T., Jacques, A., Burch, J., Gliese, U., Saito, Y., et al. (2016). Fast plasma investigation for magnetospheric multiscale. *Space Science Reviews*, *199*(1), 331–406. https://doi.org/10.1007/s11214-016-0245-4

Price, L., Swisdak, M., Drake, J. F., Cassak, P. A., Dahlin, J. T., & Ergun, R. E. (2016). The effects of turbulence on three-dimensional magnetic reconnection at the magnetopause. *Geophysical Research Letters*, *43*, 6020–6027. https://doi.org/10.1002/2016GL069578

Sauvaud, J.-A., Lundin, R., Rème, H., McFadden, J. P., Carlson, C., Parks, G. K., et al. (2001). Intermittent thermal plasma acceleration linked to sporadic motions of the magnetopause, first cluster results. *Annales Geophysicae*, *19*(10/12), 1523–1532. https://doi.org/10.5194/angeo-19-1523-2001

Scudder, J. D., Mozer, F. S., Maynard, N. C., & Russell, C. T. (2002). Fingerprints of collisionless reconnection at the separator, I, ambipolar-hall signatures. *Journal of Geophysical Research*, *107*(A10), SMP 13–1–SMP 13–38. https://doi.org/10.1029/2001JA000126

Shay, M. A., Phan, T. D., Haggerty, C. C., Fujimoto, M., Drake, J. F., Malakit, K., et al. (2016). Kinetic signatures of the region surrounding the X line in asymmetric (magnetopause) reconnection. *Geophysical Research Letters*, *43*, 4145–4154. https://doi.org/10.1002/2016GL069034

Speiser, T. W. (1965). Particle trajectories in model current sheets, 1, analytical solutions. *Journal Geophysical Research*, *70*, 4219–4226.

Toledo-Redondo, S., André, M., Khotyaintsev, Y. V., Lavraud, B., Vaivads, A., Graham, D. B., et al. (2017). Energy budget and mechanisms of cold ion heating in asymmetric magnetic reconnection. *Journal of Geophysical Research: Space Physics*, *122*, 9396–9413. https://doi.org/10.1002/2017JA024553

Toledo-Redondo, S., André, M., Khotyaintsev, Y. V., Vaivads, A., Walsh, A., Li, W., et al. (2016). Cold ion demagnetization near the X-line of magnetic reconnection. *Geophysical Research Letters*, *43*, 6759–6767. https://doi.org/10.1002/2016GL069877

Toledo-Redondo, S., André, M., Vaivads, A., Khotyaintsev, Y. V., Lavraud, B., Graham, D. B., et al. (2016). Cold ion heating at the dayside magnetopause during magnetic reconnection. *Geophysical Research Letters*, *43*, 58–66. https://doi.org/10.1002/2015GL067187

Toledo-Redondo, S., Dargent, J., Aunai, N., Lavraud, B., André, M., Li, W., et al. (2018). Perpendicular current reduction caused by cold ions of ionospheric origin in magnetic reconnection at the magnetopause: Particle-in-cell simulations and spacecraft observations. *Geophysical Research Letters*, *45*, 10,033–10,042. https://doi.org/10.1029/2018GL079051

Toledo-Redondo, S., Vaivads, A., André, M., & Khotyaintsev, Y. V. (2015). Modification of the Hall physics in magnetic reconnection due to cold ions at the Earth's magnetopause. *Geophysical Research Letters*, *42*, 6146–6154. https://doi.org/10.1002/2015GL065129

Walsh, B. M., Phan, T. D., Sibeck, D. G., & Souza, V. M. (2014). The plasmaspheric plume and magnetopause reconnection. *Geophysical Research Letters*, *41*, 223–228. https://doi.org/10.1002/2013GL058802

Walsh, B. M., Sibeck, D. G., Nishimura, Y., & Angelopoulos, V. (2013). Statistical analysis of the plasmaspheric plume at the magnetopause. *Journal of Geophysical Research: Space Physics*, *118*, 4844–4851. https://doi.org/10.1002/jgra.50458

Wang, S., Chen, L.-J., Hesse, M., Bessho, N., Gershman, D. J., Dorelli, J., et al. (2016). Two-scale ion meandering caused by the polarization electric field during asymmetric reconnection. *Geophysical Research Letters*, *43*, 7831–7839. https://doi.org/10.1002/2016GL069842

Zenitani, S., Hasegawa, H., & Nagai, T. (2017). Electron dynamics surrounding the X line in asymmetric magnetic reconnection. *Journal of Geophysical Research: Space Physics*, *122*, 7396–7413. https://doi.org/10.1002/2017JA023969